

Chiral spin liquid on a Shastry-Sutherland Heisenberg antiferromagnet

Jian-Wei Yang,^{1,*} Wei-Wei Luo,^{2,3,*} W. Zhu,^{2,3} L. Wang,⁴ Bo Yang,⁵ and Pinaki Sengupta⁵


¹*School of Microelectronics and Data Science, Anhui University of Technology, Maanshan 243002, China*

²*Institute of Natural Sciences, Westlake Institute for Advanced Study, Hangzhou 310024, China*

³*School of Science, Westlake University, Hangzhou 310024, China*

⁴*Department of Physics, Zhejiang University, Hangzhou 310000, China*

⁵*School of Physical and Mathematical Sciences, Nanyang Technological University, Singapore 637371*

 (Received 19 November 2023; revised 29 February 2024; accepted 12 April 2024; published 3 May 2024)

We demonstrate the existence of a topological chiral spin liquid in the frustrated Shastry-Sutherland Heisenberg model with an additional spin chirality interaction, using numerically unbiased exact diagonalization and density matrix renormalization group methods. We establish a quantum phase diagram where conventional phases, including dimer singlet, plaquette singlet, Néel, and collinear phase, can be clearly identified by suitable local order parameters. Among them, an $SU(2)_1$ chiral spin liquid emerges in the highly frustrated region, which is unambiguously identified by two topologically degenerate ground states, a modular matrix, and characteristic level counting in an entanglement spectrum, featuring the same topological order of the $\nu = 1/2$ bosonic Laughlin state. The phase boundaries among the different orders are determined by the energy level crossing analysis and wave-function fidelity susceptibility.

DOI: [10.1103/PhysRevB.109.205111](https://doi.org/10.1103/PhysRevB.109.205111)

I. INTRODUCTION

As one of the most intriguing quantum phases in condensed-matter physics, quantum spin liquid (QSL) [1–4] does not form any conventional order even down to zero temperature. Consequently, such a quantum state of matter goes beyond the description of Landau’s symmetry-breaking paradigm. Interestingly, the quantum disordered QSL has a rich internal organizing pattern, and it possesses fractionalized quasiparticle excitations and long-range quantum entanglement, which has been attracting a great deal of interest in the community since the initial proposal by Anderson 50 years ago [5]. Chiral spin liquid (CSL) [6], a special type of gapped QSL that breaks time-reversal symmetry, is closely related to fractional quantum Hall liquid [7–9] and thus also exhibits nontrivial topological order [10]. For the fractional quantum Hall system, gapped ground states have a topological degeneracy that depends on the lattice geometry, quasiparticle excitations possess fractional statistics, and gapless edge excitations exhibit a characteristic level counting that manifests underlying topological order in the bulk. These unique features can be used to identify topological ordered phases including CSL. Over the past decade, CSL has been unambiguously demonstrated in various lattice spin models by large-scale numerical methods, including those on a kagome lattice [11–14], a triangular lattice [15,16], a honeycomb lattice [17–19], and a square lattice [18,20,21]. Quite recently, emergent CSL has also been reported in the half-filled triangular Hubbard model [22,23], sandwiched between the metallic and Mott insulating phases. Doping in such a state may lead to superconductivity. The mechanism of the formation of CSL is

attributed to the strong interplay of geometric frustration and quantum fluctuation, which serves as a guiding principle to search for CSL in realistic models and materials.

In addition to the aforementioned widely studied lattice models, another lattice system with intrinsic frustration is the Heisenberg antiferromagnetic model on the Shastry-Sutherland (SS) lattice [24] with interdimer J and intradimer J' interactions (see the inset of Fig. 1). The SS lattice can be realized by the compound $SrCu_2(BO_3)_2$ [25,26], where in-plane spin-1/2 Cu spins are coupled by Heisenberg interactions. Interestingly, the relative strengths of these two couplings can be tuned by applying suitable pressure in experiment. Under ambient pressure, intradimer interaction dominates and a dimer singlet (DS) phase is realized [26,27]. The Néel order has also been observed at high pressure, while some variant of the plaquette singlet (PS) phase is detected around 2 GPa [28–34]. These properties of $SrCu_2(BO_3)_2$ are well captured by the phase diagram of the SS model. It is usually believed that the phase transition between the PS and Néel phase is direct [35,36], and the transition point could even be a deconfined quantum critical point (DQCP) [32,37]. However, some recent numerical studies on the SS model suggested the possibility of an intermediate gapless spin liquid between the PS phase and the Néel phase [38–40]. Since $SrCu_2(BO_3)_2$ can be fabricated quite cleanly in experiment, the disorder effect is quite small, which makes it promising to explore the possibility of a gapless spin liquid. It is thus also important to study some variants of the SS model to find gapped spin liquids, which will guide the experimental discovery of such exotic phases. This is the motivation of this paper.

In this paper, we demonstrate the existence of a topologically ordered CSL in the highly frustrated region of the SS model. Specifically, we consider antiferromagnetic Heisenberg interactions in the original SS model, as well as an

*These authors contributed equally to this work.

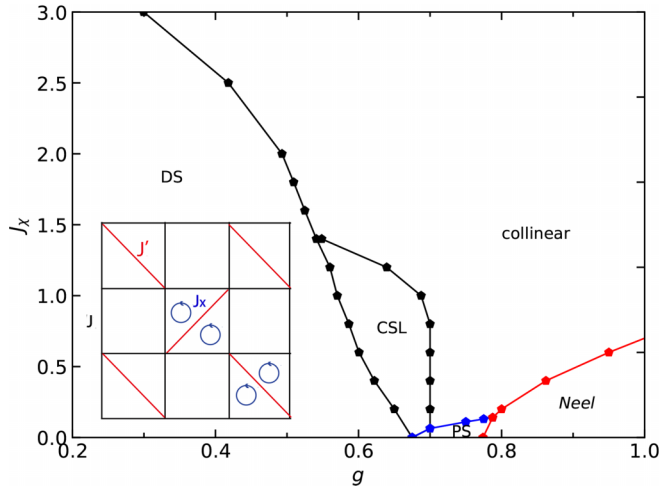


FIG. 1. Quantum phase diagram vs $J_\chi - g$ of the antiferromagnetic Heisenberg model on the SS lattice. The phase boundaries are based from fidelity susceptibility and energy level crossing on a 36-site torus using the ED method. The inset shows the schematic plot of the SS lattice, with NN J (denoted as black lines) and NNN J' (denoted as red lines) Heisenberg interactions, and a three-site chiral interaction (denoted as blue circles) in plaquettes with a J' term [see Eq. (1)].

additional spin chirality interaction. Using large-scale ED and DMRG calculations [41,42], we establish a global phase diagram with various conventional phases identified by local order parameters, including nonmagnetic DS and PS phases, and magnetic Néel and collinear phases. Moreover, among the phase boundaries of these conventionally ordered phases, there exists a CSL state. This CSL possesses two topologically degenerate ground states, and it is characterized by a modular matrix [10,43] and sequential level countings in an entanglement spectrum [44] as the fingerprints of the $\nu = 1/2$ bosonic Laughlin state processing semion anyonic statistics.

II. MODEL AND METHOD

As is illustrated in the inset of Fig. 1, we study the SS model with an additional spin chirality interaction on a square lattice, with the Hamiltonian

$$H = J \sum_{\langle ij \rangle} \mathbf{S}_i \cdot \mathbf{S}_j + J' \sum_{\langle ij \rangle'} \mathbf{S}_i \cdot \mathbf{S}_j + J_\chi \sum_{ijk \in \Delta} \mathbf{S}_i \cdot (\mathbf{S}_j \times \mathbf{S}_k), \quad (1)$$

where antiferromagnetic Heisenberg interactions J and J' run over all nearest-neighbor (NN) bonds $\langle ij \rangle$ and specific next-nearest-neighbor (NNN) bonds $\langle ij \rangle'$, respectively. The first two terms of Eq. (1) constitute the canonical SS model, which is widely accepted as the microscopic Hamiltonian describing the dominant magnetic interactions in $\text{SrCu}_2(\text{BO}_3)_2$. The real material also features additional interactions (e.g., strong spin-orbit coupling) that has motivated the generalization of the canonical SS model to include (effective) realistic interactions. In the present study, we consider a three-site spin chiral interaction with strength J_χ , which runs over the two triangles in each plaquette with a J' bond, where the sites ijk are ordered in a counterclockwise manner. Chiral inter-

actions normally arise from the coupling of electrons to an external magnetic field in strong Mott insulators, particularly in lattice geometries with triangular units [13,45–48]. These interactions break reflection (mirror-plane) and time-reversal symmetries, but their product is preserved, as are translational and rotational symmetries. In the following, we define $g \equiv J/J'$ and set $J' = 1$ as the energy scale.

Here we use numerically unbiased ED and DMRG methods to study this model, which allows us to faithfully explore possible quantum phases and phase transitions in strongly correlated systems. Using a torus geometry in the ED calculation, we examine different system symmetries and block-diagonalize the Hamiltonian in different symmetry sectors labeled by conserved quantum numbers. This allows us to achieve larger system sizes in ED, and more importantly to detect intriguing phase transitions using energy level crossings. In the following, we obtain the low-lying energy spectrum and label each state with quantum numbers (S, k_x, k_y, r) , where S is the total spin quantum number, k_x and k_y label lattice momenta in the x and y directions, respectively, and r is the quantum number of the C_4 rotational symmetry. We can thus obtain an approximate phase diagram based on energy level crossing and fidelity susceptibility. Different order parameters are further utilized to identify the nature of quantum phases in the phase diagram. Furthermore, We find a finite region of CSL at intermediate g , whose topological order is elaborately characterized by both ED and DMRG calculations. Compared with the ED method, DMRG allows us to study much larger system sizes in a cylindrical geometry, and quantum entanglement can be straightforwardly extracted from the ground state.

III. PHASE DIAGRAM

In this section, we summarize our main results and present a global quantum phase diagram of the model in Fig. 1, which is based on a 36-site torus geometry using the ED method. Detailed discussions of quantum phases and phase transitions will be presented in subsequent sections.

When the chiral interaction is turned off, the model returns to the well-studied SS model. At small g , the intradimer J' term dominates and the system favors the DS phase, where each separate bond connected by the J' term forms a spin singlet to simultaneously minimize system energy. At the large- g limit, the Hamiltonian reduces to the antiferromagnetic Heisenberg model on a square lattice, whose ground state possesses the conventional Néel order [49]. In the intermediate region, J and J' interactions compete with each other, and the SS model is highly frustrated. In this case, nonmagnetic phases with unconventional properties may also emerge. In our 36-site ED calculation, we find a PS phase for $g \in (0.675, 0.774)$, which evolves to a DS phase and a Néel phase for small and large g , respectively. Recent calculations with careful finite-size extrapolation have also suggested the possibility of an intermediate gapless spin liquid between the PS and Néel phases [38].

Next we investigate the effect of the nonzero J_χ interaction. The result of our investigation is summarized in Fig. 1. At small to moderate values of g ($\lesssim 0.5$), the ground state remains in the DS phase up to strong values of J_χ , but eventually

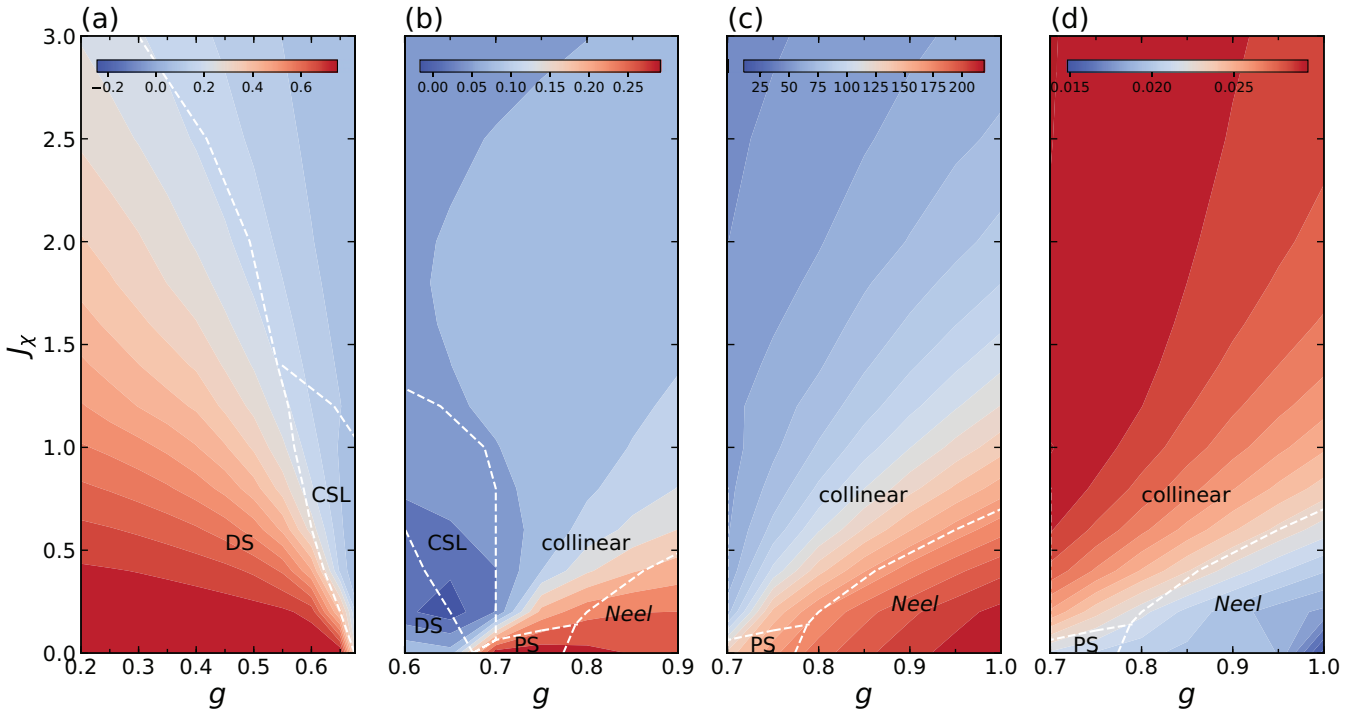


FIG. 2. Profile of various order parameters measured in the quantum phase diagram. Here we study an $N = 36$ -site torus by the ED method. (a) Dimer order parameter O_d , (b) plaquette order parameter O_p , (c) Néel order parameter $m^2(\pi, \pi)$, and (d) collinear order parameter $m^2(0, \pi)$. Dashed lines mark the same phase boundaries as in Fig. 1.

there is a transition to a collinear phase at large J_χ . On the other hand, the Néel phase (at large g) survives for small to intermediate values of J_χ , beyond which the collinear order sets in. The PS phase is the most unstable to the effects of chiral interaction and survives only for small values of J_χ . It is at intermediate values of g ($0.5 \lesssim g \lesssim 0.7$) that the most interesting physics emerge. We find clear signatures of the CSL phase over a finite range of J_χ for these values of g where interactions are highly frustrated. The emergence of a CSL when turning on the chiral interaction in a highly frustrated region has also been observed in a number of lattice systems of a Heisenberg antiferromagnet, including kagome [13], triangular [15], and square lattice systems [20]. Recent numerical studies also report the appearance of non-Abelian CSLs in higher spin systems on the square lattice [50,51]. Interestingly, while the CSL phase is driven by the chiral interaction, it requires the competing Heisenberg interactions for stabilization. For example, the CSL phase does not emerge in the presence of only the J_χ term in the Hamiltonian; instead, the collinear phase is realized in this limit.

IV. CONVENTIONAL ORDERS

Various conventional phases in the phase diagram can be effectively identified by suitably chosen local order parameters. First, since the dimer phase is defined by the spin singlet formed along J' -bonds, we define a dimer order parameter as the difference between the averaged expectation value $\langle \mathbf{S}_i \cdot \mathbf{S}_j \rangle$ for NN J bonds and NNN J' bonds as

$$\mathbf{O}_d = E_J - E_{J'}. \quad (2)$$

The DS phase in the original SS model is an exact dimer phase, which exhibits a finite value of $\mathbf{O}_d = 0.75$ [36,52]. When $J_\chi > 0$, the DS phase is destroyed gradually, with \mathbf{O}_d decreasing and potentially becoming negative. As is shown in Fig. 2(a), O_d is quite large for a relatively small g regime, and the region for $J_\chi = 0$ with large O_d coincides with the DS phase determined by another way [38].

Second, we define a plaquette order parameter as

$$\begin{aligned} \mathbf{O}_p &= \frac{1}{2}(\mathbf{P}_\square + \mathbf{P}_\square^{-1}) \\ &= -\frac{5}{8} + \frac{1}{4}(\mathbf{S}_i + \mathbf{S}_j + \mathbf{S}_k + \mathbf{S}_l)^2 + 2(\mathbf{S}_i \cdot \mathbf{S}_j)(\mathbf{S}_k \cdot \mathbf{S}_l) \\ &\quad + 2(\mathbf{S}_i \cdot \mathbf{S}_l)(\mathbf{S}_j \cdot \mathbf{S}_k) - 2(\mathbf{S}_i \cdot \mathbf{S}_k)(\mathbf{S}_j \cdot \mathbf{S}_l), \end{aligned} \quad (3)$$

where \mathbf{P}_\square is a clockwise permutation operator that acts on the plaquette without a J' bond, and $\{i, j, k, l\}$ are indicators of a clockwise arrangement on the four vertices of the plaquette. \mathbf{O}_p represents the strength of the plaquette, which can be used to identify the PS phase. In Fig. 2(b), we find that the plaquette order takes a large value in a window for intermediate g . By increasing J_χ , the plaquette order decreases monotonically, which shows that the plaquette order is not favored by the spin chirality term. However, it is hard to distinguish the PS and Néel phases from \mathbf{O}_p . One reason is PS-Néel is a continuous [37] (or weakly first-order [36,53]) phase transition, and another reason is that the lattice size is still too small.

Third, in addition to the two kinds of dimer phases, we also calculate the static structure factor to identify possible long-range magnetic orders in the phase diagram, defined as

$$m^2(k_x, k_y) = \frac{1}{N^2} \sum_{ij} e^{i\mathbf{k} \cdot (\mathbf{r}_i - \mathbf{r}_j)} \langle \mathbf{S}_i \cdot \mathbf{S}_j \rangle. \quad (4)$$

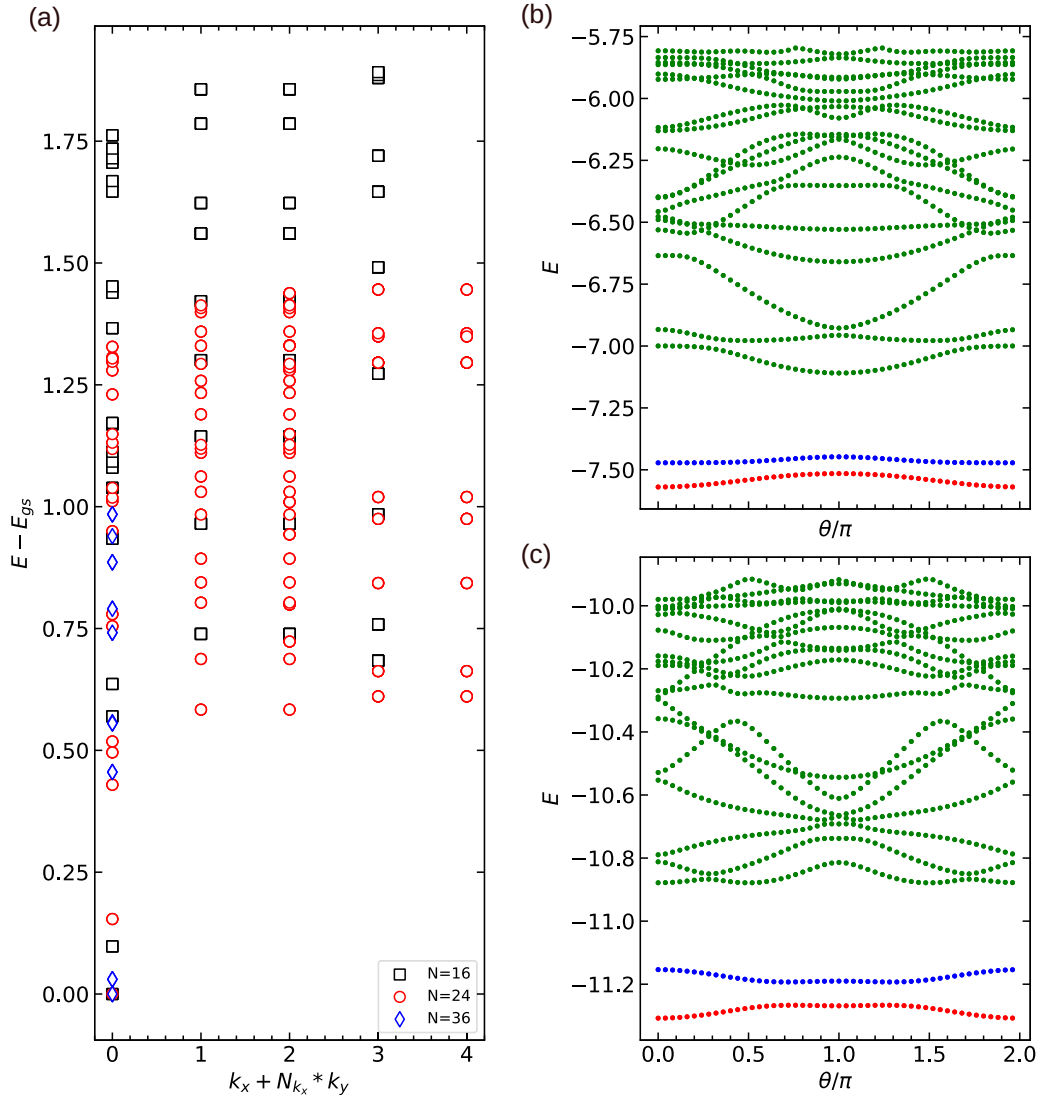


FIG. 3. Energy spectrum and spectral flow of the CSL phase. (a) Low-energy spectra $E_n - E_1$ vs the momentum $k_x + N k_x * k_y$ in the CSL phase for lattice sizes $N = 16, 24$, and 36 at $(g, J_\chi) = (0.6, 0.75)$, where a large gap exists between two ground states and other excited states in all studied lattice sizes. Panels (b) and (c) are low-energy spectra vs inserted flux θ at $(g, J_\chi) = (0.6, 0.75)$ for $N = 16$ and 24 , respectively, where the two topologically degenerate ground states (marked as red and blue points) remain well separated from higher energy levels (marked as green points) on flux insertion.

A peak at $\mathbf{k} = (k_x, k_y) = (\pi, \pi)$ corresponds to antiferromagnetic Néel order, while that at $(\pi, 0)$ or $(0, \pi)$ signals the formation of collinear order. In particular, $m^2(k_x, k_y)$ at $\mathbf{k} = (k_x, k_y) = (\pi, \pi)$ is also called squared magnetization. The results of $m^2(\pi, \pi)$ and $m^2(0, \pi)$ are shown in Figs. 2(c) and 2(d), respectively.

In Figs. 2(a)–2(d), we find a large value of O_p , $m^2(\pi, \pi)$, $m^2(0, \pi)$ at the PS, Néel, and collinear phase, respectively. These distributions of order parameters in the phase diagram in Fig. 2 generally agree with the phase diagram presented in Fig. 1.

V. CHIRAL SPIN LIQUID

Among these conventional phases characterized by local order parameters, we find a finite region of CSL in the quantum phase diagram where competing interactions are highly

frustrated. This spin-disordered phase cannot be characterized by conventional order parameters, but by its intriguing topological order. Next, we will demonstrate the numerical evidence from the viewpoints of energy spectra, entanglement spectra, and modular matrix.

A. Energy spectra

First, we find twofold topologically degenerate ground states, which are well separated from bulk excitations with a large energy gap, as is shown in Fig. 3(a) for the CSL phase of lattice sizes $N = 16, 24$, and 36 at $(g, J_\chi) = (0.6, 0.75)$. This excitation gap remains robust when adiabatically twisting the boundary condition, i.e., the twofold ground states never cross with the excited states. Since the twofold ground states share the same momentum quantum numbers in these three high-symmetric lattice clusters, the energy spectrum evolves back

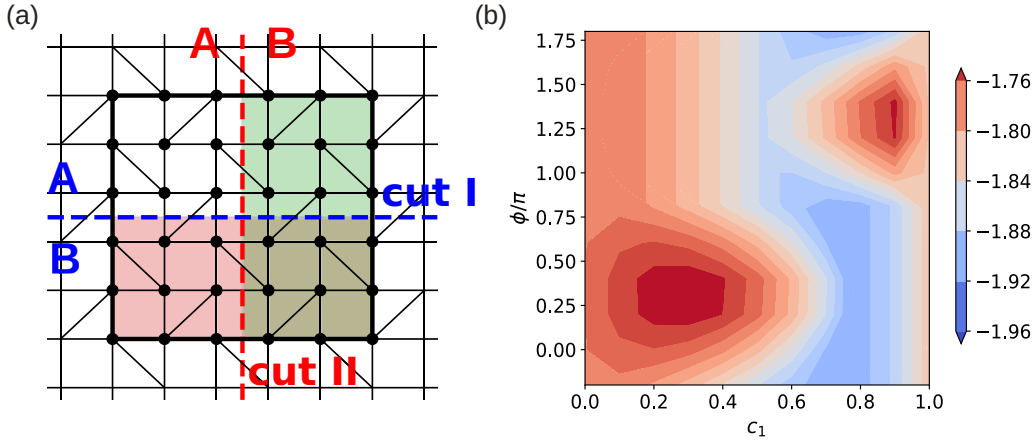


FIG. 4. (a) Bipartitions of the SS model system on a $N = 36$ cluster. The two ways to partition the system along the dashed lines are labeled as cut I and cut II , respectively. (b) Profile of minus entanglement entropy ($-S$) of wave function $|\Phi_{c_1, \phi}\rangle$ on the $N = 36$ lattice with $g = 0.6$ and $J_x = 0.75$. These two peaks correspond to minimally entangled states along bipartition cut I , which are used in the calculation of modular matrix.

to itself by inserting a flux quantum, as is shown in Figs. 3(b) and 3(c) for $N = 16$ and 24 , respectively.

B. Fractional statistics

An important feature of a topological ordered state is that its quasiparticle excitation takes the fractional statistics. Here we utilize the framework of modular matrices [10,43], which encode complete information of topological order, to characterize the underlying anyon statistics of the CSL. Interestingly, modular matrices can be effectively obtained from entanglement measurements [54,55]. Given the topologically degenerate ground states on a torus geometry, we construct two sets of minimally entangled states (MESs) along interwinding cuts, and the transformation between these two MES sets yields desired modular matrices.

To construct MESs, we take an arbitrary superposition of the ground states $|\xi_1\rangle$ and $|\xi_2\rangle$,

$$|\Phi_{c_1, \phi}\rangle = c_1|\xi_1\rangle + c_2e^{i\phi}|\xi_2\rangle, \quad (5)$$

where c_1 and ϕ are two independent real numbers, and $c_2 = \sqrt{1 - c_1^2}$. We bipartite the whole system into two parts, A and B , and we construct the reduced density matrix of subsystem A by tracing out degrees of freedom in subsystem B as $\rho_A = \text{Tr}_B |\Phi_{c_1, \phi}\rangle\langle\Phi_{c_1, \phi}|$, such that the entanglement entropy for this cut is obtained by $S = -\log \text{Tr} \rho_A^2$. By evaluating S for each linear combination of the ground states, we identify (c_1, ϕ) pairs corresponding to states with minimal entanglement entropy, i.e., MESs. As is shown in Fig. 4(a), we use two ways to bipartite the system along noncontractible cuts I and II , each yielding one set of MESs. In Fig. 4(b), we draw the profile of $-S$ as a function of (c_1, ϕ) in the contour plot for a 36-site lattice, so that the peaks represent the minima of S . In this way, we identify two peaks in (c_1, ϕ) parameter space, corresponding to two distinct MESs:

$$\begin{aligned} |\Xi_1^I\rangle &= 0.897|\xi_1\rangle + 0.442e^{i1.374\pi}|\xi_2\rangle, \\ |\Xi_2^I\rangle &= 0.295|\xi_1\rangle + 0.955e^{i0.371\pi}|\xi_2\rangle, \end{aligned} \quad (6)$$

where the label I means we bipartite the system along the horizontal line (cut I). We find that the relative phase difference between these two MESs is $\phi(1) - \phi(2) = \pi$, and consequently the two MESs are approximately orthogonal to each other for this finite-size system: $|\langle\Xi_1^I|\Xi_2^I\rangle| \approx 0.169$. Due to the $\pi/2$ rotation symmetry in the system, the MESs along the vertical line (cut II) $|\Xi_i^{II}\rangle$ are related to $|\Xi_i^I\rangle$ as $|\Xi_i^{II}\rangle = R_{\pi/2}|\Xi_i^I\rangle$, where $R_{\pi/2}$ rotates a state anticlockwise by $\pi/2$.

In our calculation, we identify that

$$\begin{aligned} R_{\pi/2}|\xi_1\rangle &= |\xi_1\rangle, \\ R_{\pi/2}|\xi_2\rangle &= -|\xi_2\rangle, \end{aligned} \quad (7)$$

and then we have the second set of MESs,

$$\begin{aligned} |\Xi_1^{II}\rangle &= 0.897|\xi_1\rangle - 0.442e^{i1.374\pi}|\xi_2\rangle, \\ |\Xi_2^{II}\rangle &= 0.295|\xi_1\rangle - 0.955e^{i0.371\pi}|\xi_2\rangle. \end{aligned} \quad (8)$$

Finally we get the modular matrix by $S = \langle\Xi^{II}|\Xi^I\rangle$ as

$$S \approx 0.7176 \begin{pmatrix} 0.8490 & 0.9713 \\ 0.9713 & -1.1510 \end{pmatrix}, \quad (9)$$

which is close to the analytic prediction for the bosonic $\nu = 1/2$ Laughlin state [56–58]:

$$S = \frac{1}{\sqrt{2}} \begin{pmatrix} 1 & 1 \\ 1 & -1 \end{pmatrix}. \quad (10)$$

This directly shows the semion statistics emergent in the CSL.

C. Entanglement spectra

To establish the existence of CSL conclusively, we have studied larger systems, up to $L_y \times L_x = 8 \times 16$ with a cylindrical lattice using DMRG for a representative set of parameters for which the ground state is in the CSL phase. Various entanglement information of the ground state can be straightforwardly extracted in this method. To reveal the underlying topological order, we calculate the entanglement spectrum [44] from the entanglement Hamiltonian $-\log \rho_A$,

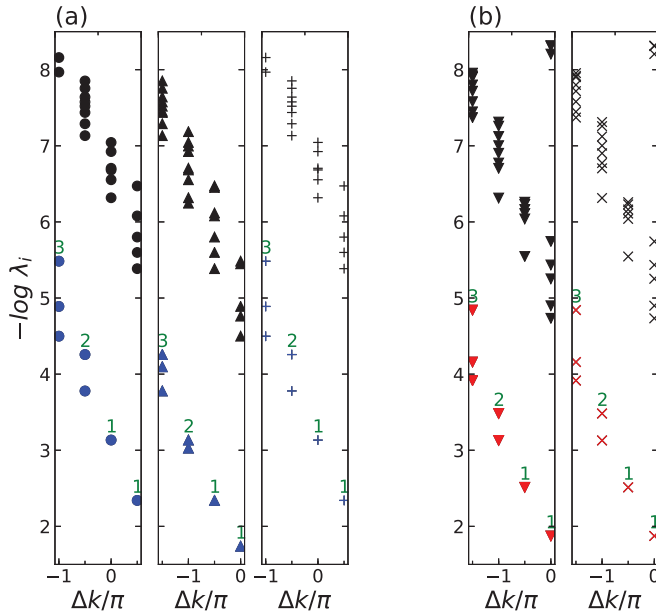


FIG. 5. Momentum-resolved entanglement spectra of the two ground states at $(g, J_\chi) = (0.6, 0.75)$ on the 8×16 cylinder, where Δk means relative momentum in the transverse direction of the cylinder, and λ_i represents the eigenvalues of reduced density matrix ρ_A . Here we set $\Delta k = 0$ for the largest λ_i . Panels (a) and (b) correspond to the ground state at the vacuum and semion sector, respectively. These counting structures at different S^z sectors match the tower of states of $SU(2)_1$ Wess-Zumino-Witten theory.

whose low-lying spectrum $\{-\log \lambda_i\}$ harbors characteristic edge countings for topologically ordered phases.

In the DMRG optimization, we get one of the ground states directly and the other one by the removal of a single site at each edge. We keep up to 1200 $U(1)$ states to obtain accurate results with the truncation error less than 10^{-6} . The entanglement spectra of the ground states are presented in Fig. 5. The degeneracy pattern in the low-lying entanglement spectrum $\{1, 1, 2, 3, 5, \dots\}$ follows the $U(1)$ decomposition of the $SU(2)_1$ Wess-Zumino-Witten CFT theory [59] exactly, establishing the same topological order as in the $\nu = 1/2$ bosonic Laughlin state. Intuitively, this counting structure can also be simply obtained by the generalized Pauli principle [60], which states that there is no more than one particle in two consecutive orbitals in this case.

VI. PHASE BOUNDARIES

In this section, we determine the phase boundaries between the various ground-state phases in Fig. 1, based on energy level crossing and fidelity susceptibility numerically using the ED method on a 36-site torus. To get the phase boundaries, we fix J_χ and change g . As examples, the results of $J_\chi = 0.4$ and 2.0 are shown in Fig. 6. All states $|\phi\rangle$ are labeled by quantum numbers (S, k_x, k_y, r) . In our results, the low-lying states in the level spectroscopy are mainly located in the $r = 0$ and $r = \pi$ sectors, where $r = 0$ means the states satisfy $R_{\pi/2}|\phi\rangle = |\phi\rangle$, while $r = \pi$ means $R_{\pi/2}|\phi\rangle = -|\phi\rangle$.

The fidelity susceptibility (FS) that we use here is defined as

$$\chi_F(g) \equiv \lim_{\delta g \rightarrow 0} \frac{-2 \ln F}{(\delta g)^2} = -\frac{\partial^2 F}{\partial (\delta g)^2}, \quad (11)$$

where $F = |\langle \phi(g + \delta g) | \phi(g) \rangle|$ is the definition of fidelity, and $\phi(g)$ is the ‘‘ground state’’ of a given singlet sector at parameter g . We compute FS in both $(S = 0, 0, 0, 0)$ and $(S = 0, 0, 0, \pi)$ sectors, which are shown in Figs. 6(e) and 6(f). When a quantum phase transition occurs, $\phi(g)$ undergoes a significant change at a certain point, and the fidelity F deviates from 1, leading to a peak on the FS curve.

The FS approach is effective in detecting quantum phase transitions [61–63]. With this approach, we obtain the DS-CSL, DS-collinear, and CSL-collinear phase boundaries, i.e., the black curves in Fig. 1. However, for certain types of quantum phase transitions, such as the PS-Néel transition in the original SS model ($J_\chi = 0$), there are no peaks on the fidelity curves and the FS approach fails.

For this reason, we use excited energy level crossings to get the PS-Néel, PS-collinear, and Néel-collinear phase boundaries, i.e., the red and blue curves in Fig. 1. From this point of view, quantum phases have their own characteristic energy spectra, which is usually called a tower of states (TOS), and the quantum phase transitions are caused by the reconstruction of the TOS. During the reconstruction, the crossing point of low-lying excited energy levels provides an approximate quantum critical point at a finite size. This method has been widely applied to various different systems [38,40,64–71].

In the study of the square lattice and the SS lattice, both FS and level crossing methods have also been successfully applied in Refs. [38,40,66]. Below we will present a detailed discussion on Fig. 6.

We first review the phase transitions in the original SS model at $J_\chi = 0$. The energy evolution of the ground states on increasing NN Heisenberg interaction J (or equivalently g) is easily understood. The two lowest singlet ($S = 0$) energy levels cross with each other and change their order at $g \approx 0.675$. For small $g \lesssim 0.675$, the global ground state has a relatively fixed energy on varying g , which is a typical character of the DS phase. In this case, the ground state is mainly a product state of spin singlets, with each bond connected by the J' term. As a result, the typical ground-state energy is thus $-0.75N_s$. For $g \gtrsim 0.675$ the global ground state instead changes to other phases, namely the PS phase and the Néel phase in this region [35–37,52]. (It was argued recently that there may also be an intermediate gapless spin-liquid phase between the PS and Néel phases [38,40].) Energy level crossing may be the most effective approach to distinguish the PS and Néel phases, since the low-lying states of the Néel phase are the famous Anderson TOS, while the ground states of PS have a twofold degeneracy [35,72]. The lowest excitation of the Néel phase is a triplet state, while it is a singlet state for the collinear phase. We can use the singlet ($S = 0$)-triplet ($S = 1$) crossing point as the boundary of the PS phase in a small cluster. This point is also in strong agreement with the iPEPS [36] and iDMRG [37] results [38].

However, as is shown in Figs. 6(a) and 6(c), the energy spectras at $J_\chi = 0.4$ are markedly different. For $g \lesssim 0.625$, the ground state is still a DS phase, and the peak at $g \approx 0.625$

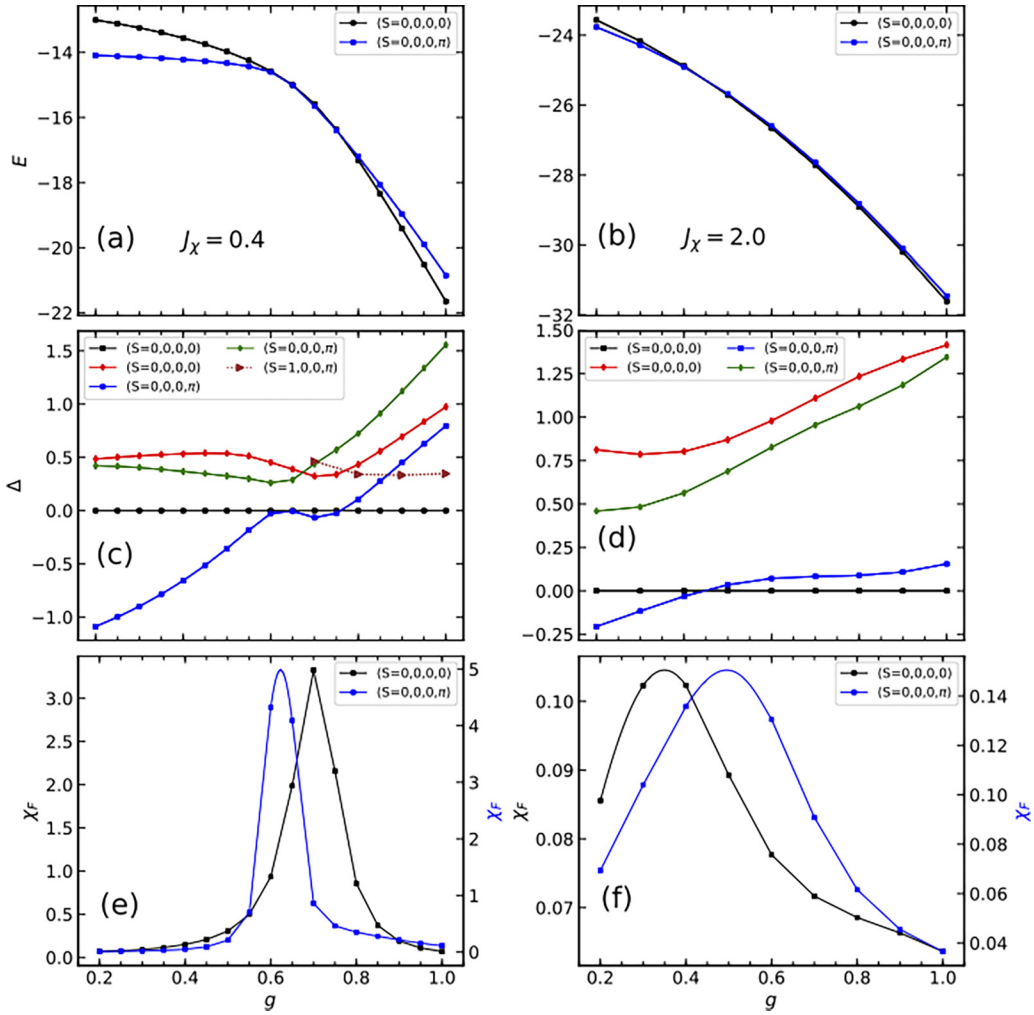


FIG. 6. Level spectroscopy at $J_\chi = 0.4$ and 2.0 in (a) and (b), respectively, by varying J_2 for the $N = 36$ periodic cluster. The two lowest singlets are displayed for both the $(S = 0, 0, 0, 0)$ sector (in black squares and red pentagons) and the $(S = 0, 0, 0, \pi)$ sector (in blue squares and green pentagons). Characteristic magnetic excitations of the Néel phase are also shown, i.e., Anderson tower excitation in terms of the $(S = 1, 0, 0, \pi)$ triplet (in purple triangles). Energy gaps defined with respect to the lowest $(S = 0, 0, 0, 0)$ singlet are shown in (c) and (d) for $J_\chi = 0.4$ and 2.0 , respectively. For the lowest $(S = 0, 0, 0, 0)$ singlet and the lowest $(S = 0, 0, 0, \pi)$ singlet state, the corresponding FSs are shown in (e) and (f).

of the FS curve in the $(S = 0, 0, 0, \pi)$ sector [see Fig. 6(e)] forms a boundary of DS. When $g > 0.625$, there is a finite range of g over which the two ground states in the $(S = 0, 0, 0, 0)$ and $(S = 0, 0, 0, \pi)$ sectors are nearly degenerate, and they turn out to be the topologically degenerate ground states of the CSL phase. In Fig. 6(e), the FS curve of the ground state in the $(S = 0, 0, 0, 0)$ sector indicates a phase transition at $g = 0.7$, which becomes a phase boundary of the CSL phase. Further increasing g leads to two magnetic orders, i.e., collinear order and Néel order. They are separated by the singlet-triplet level crossing point at $g = 0.862$, which is displayed in Fig. 6(c). Since the low-lying states of Néel order form the Anderson TOS, the lowest excitation is a triplet state in the $(S = 0, 0, 0, \pi)$ sector, while for collinear order the lowest excitation is one of the twofold-degenerate ground states, which is a singlet state in the $(S = 0, 0, 0, \pi)$ sector.

When J_χ is 2.0 , the ground state is still the DS state in the $(S = 0, 0, 0, \pi)$ sector while g is small. With the increase of g , the state in the $(S = 0, 0, 0, \pi)$ sector has a FS peak at $g \approx$

0.5 , as shown in Fig. 6(f). At the same time, there is a crossing point between the $(S = 0, 0, 0, 0)$ and $(S = 0, 0, 0, \pi)$ curves at $g = 0.45$ [see Fig. 6(d)]. Both points can be regarded as the DS-collinear phase boundary, but they are not consistent due to the finite-size effect. To maintain consistency with the case of $J_\chi = 0.4$, we select the FS peak at $g \approx 0.5$ as the phase boundary. As in Fig. 6(e), in Fig. 6(f) both the $(S = 0, 0, 0, 0)$ sector and the $(S = 0, 0, 0, \pi)$ sector have a FS peak. However, the phase boundaries presented in these two figures are completely different. In Fig. 6(f), the FS peak of the $(S = 0, 0, 0, 0)$ curve is located at $g = 0.35$, indicating a phase transition of the excited state of the DS phase, but only when $g > 0.5$ will the corresponding states of the $(S = 0, 0, 0, 0)$ and $(S = 0, 0, 0, \pi)$ sectors form the twofold degeneracy of the collinear phase.

To pin down the phase boundary of the PS phase, we fix g and instead change J_χ . In Fig. 7(a) we show the evolution of three low-lying energy levels upon increasing the chiral interaction at $g = 0.775$. At small J_χ the system is in the PS

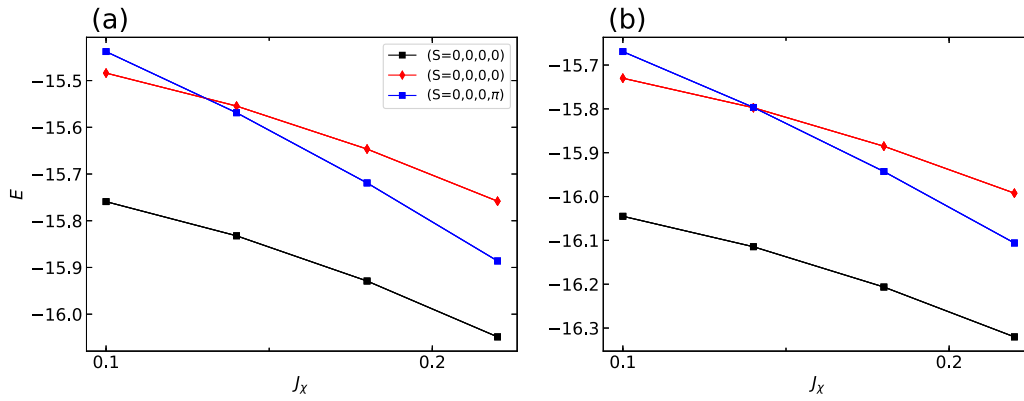


FIG. 7. Level spectroscopy at $g = 0.775$ and 0.7875 in (a) and (b), respectively, by varying J_x for an $N = 36$ periodic cluster. The two lowest singlets in the $(S = 0, 0, 0, 0)$ sector are displayed in black squares and red pentagons, respectively, and the lowest singlet in the $(S = 0, 0, 0, \pi)$ sector is displayed in blue squares.

phase and thus the lowest two energy levels remain in the $(S = 0, 0, 0, 0)$ sector. For $J_x \gtrsim 0.13$, an excited level crossing occurs, indicating a transition to the collinear phase, where the lowest two energy levels remain in the $(S = 0, 0, 0, 0)$ and $(S = 0, 0, 0, \pi)$ sector, respectively. We also observe a similar behavior at $g = 0.7875$, where the excited level crossing occurs at $J_x \approx 0.14$.

Based on the above discussion, we establish the ground-state phase diagram as shown in Fig. 1, which is further corroborated by the results of order parameters in Fig. 2.

VII. SUMMARY AND DISCUSSION

In summary, we study the antiferromagnetic SS model with an additional three-spin chiral interaction using numerically unbiased ED and DMRG calculations. Using local order parameters, various conventional phases have been identified, including the magnetic Néel phase and the collinear phase, and the nonmagnetic DS and PS phases. The PS phase emerges when the SS model is highly frustrated, and we show that a topologically ordered CSL can emerge by

adding a small chirality interaction to this phase, which is conclusively identified as a $\nu = 1/2$ Laughlin state by a characteristic modular matrix and an entanglement spectrum. In addition, the phase transitions in the global phase diagram are determined by using energy level crossing and fidelity susceptibility, which shows a finite region of the CSL phase. Since the quantum material $\text{SrCu}_2(\text{BO}_3)_2$ is highly related to the SS model, we expect to observe CSL under certain circumstances in experiment. To be specific, the CSL exhibits electromagnetic signatures to facilitate experimental detection even within a Mott insulator regime [73], i.e., the electrical charge and orbital electrical current associated with a spinon excitation and a nonvanishing optical response.

ACKNOWLEDGMENTS

W.W.L. and W.Z. were supported by “Pioneer” and “Leading Goose” R&D Program of Zhejiang (2022SDXHDX0005), and National Natural Science Foundation of China (No. 92165102 and No. 11974288). P.S. acknowledges financial support from the Ministry of Education, Singapore through Grant No. RG 159/19.

-
- [1] L. Balents, Spin liquids in frustrated magnets, *Nature (London)* **464**, 199 (2010).
 - [2] Y. Zhou, K. Kanoda, and T.-K. Ng, Quantum spin liquid states, *Rev. Mod. Phys.* **89**, 025003 (2017).
 - [3] L. Savary and L. Balents, Quantum spin liquids: A review, *Rep. Prog. Phys.* **80**, 016502 (2017).
 - [4] C. Broholm, R. J. Cava, S. A. Kivelson, D. G. Nocera, M. R. Norman, and T. Senthil, Quantum spin liquids, *Science* **367**, eaay0668 (2020).
 - [5] P. W. Anderson, Resonating valence bonds: A new kind of insulator? *Mater. Res. Bull.* **8**, 153 (1973).
 - [6] V. Kalmeyer and R. B. Laughlin, Equivalence of the resonating-valence-bond and fractional quantum Hall states, *Phys. Rev. Lett.* **59**, 2095 (1987).
 - [7] K. v. Klitzing, G. Dorda, and M. Pepper, New method for high-accuracy determination of the fine-structure constant based on quantized Hall resistance, *Phys. Rev. Lett.* **45**, 494 (1980).
 - [8] D. C. Tsui, H. L. Stormer, and A. C. Gossard, Two-dimensional magnetotransport in the extreme quantum limit, *Phys. Rev. Lett.* **48**, 1559 (1982).
 - [9] R. B. Laughlin, Anomalous quantum Hall effect: An incompressible quantum fluid with fractionally charged excitations, *Phys. Rev. Lett.* **50**, 1395 (1983).
 - [10] X. G. Wen, Topological orders in rigid states, *Int. J. Mod. Phys. B* **04**, 239 (1990).
 - [11] S.-S. Gong, W. Zhu, and D. N. Sheng, Emergent chiral spin liquid: Fractional quantum Hall effect in a kagome Heisenberg model, *Sci. Rep.* **4**, 6317 (2014).
 - [12] Y.-C. He, D. N. Sheng, and Y. Chen, Chiral spin liquid in a frustrated anisotropic kagome Heisenberg model, *Phys. Rev. Lett.* **112**, 137202 (2014).

- [13] B. Bauer, L. Cincio, B. P. Keller, M. Dolfi, G. Vidal, S. Trebst, and A. W. W. Ludwig, Chiral spin liquid and emergent anyons in a kagome lattice Mott insulator, *Nat. Commun.* **5**, 5137 (2014).
- [14] Y.-C. He and Y. Chen, Distinct spin liquids and their transitions in spin-1/2 xxz kagome antiferromagnets, *Phys. Rev. Lett.* **114**, 037201 (2015).
- [15] S.-S. Gong, W. Zhu, J.-X. Zhu, D. N. Sheng, and K. Yang, Global phase diagram and quantum spin liquids in spin-1/2 triangular antiferromagnet, *Phys. Rev. B* **96**, 075116 (2017).
- [16] T. Cookmeyer, J. Motruk, and J. E. Moore, Four-spin terms and the origin of the chiral spin liquid in Mott insulators on the triangular lattice, *Phys. Rev. Lett.* **127**, 087201 (2021).
- [17] C. Hickey, L. Cincio, Z. Papić, and A. Paramekanti, Haldane-Hubbard Mott insulator: From tetrahedral spin crystal to chiral spin liquid, *Phys. Rev. Lett.* **116**, 137202 (2016).
- [18] C. Hickey, L. Cincio, Z. Papić, and A. Paramekanti, Emergence of chiral spin liquids via quantum melting of noncoplanar magnetic orders, *Phys. Rev. B* **96**, 115115 (2017).
- [19] Y. Huang, X.-Y. Dong, D. N. Sheng, and C. S. Ting, Quantum phase diagram and chiral spin liquid in the extended spin- $\frac{1}{2}$ honeycomb xy model, *Phys. Rev. B* **103**, L041108 (2021).
- [20] A. E. B. Nielsen, G. Sierra, and J. I. Cirac, Local models of fractional quantum Hall states in lattices and physical implementation, *Nat. Commun.* **4**, 2864 (2013).
- [21] J. Merino and A. Ralko, Majorana chiral spin liquid in a model for Mott insulating cuprates, *Phys. Rev. Res.* **4**, 023122 (2022).
- [22] A. Szasz, J. Motruk, M. P. Zaletel, and J. E. Moore, Chiral spin liquid phase of the triangular lattice Hubbard model: A density matrix renormalization group study, *Phys. Rev. X* **10**, 021042 (2020).
- [23] B.-B. Chen, Z. Chen, S.-S. Gong, D. N. Sheng, W. Li, and A. Weichselbaum, Quantum spin liquid with emergent chiral order in the triangular-lattice Hubbard model, *Phys. Rev. B* **106**, 094420 (2022).
- [24] B. S. Shastry and B. Sutherland, Exact ground state of a quantum mechanical antiferromagnet, *Physica B+C* **108**, 1069 (1981).
- [25] R. W. Smith and D. A. Keszler, Synthesis, structure, and properties of the orthoborate $\text{SrCu}_2(\text{BO}_3)_2$, *J. Solid State Chem.* **93**, 430 (1991).
- [26] H. Kageyama, K. Yoshimura, R. Stern, N. V. Mushnikov, K. Onizuka, M. Kato, K. Kosuge, C. P. Slichter, T. Goto, and Y. Ueda, Exact dimer ground state and quantized magnetization plateaus in the two-dimensional spin system $\text{SrCu}_2(\text{BO}_3)_2$, *Phys. Rev. Lett.* **82**, 3168 (1999).
- [27] S. Miyahara and K. Ueda, Exact dimer ground state of the two dimensional Heisenberg spin system $\text{SrCu}_2(\text{BO}_3)_2$, *Phys. Rev. Lett.* **82**, 3701 (1999).
- [28] M. E. Zayed, C. Rüegg, J. Larrea J., A. M. Läuchli, C. Panagopoulos, S. S. Saxena, M. Ellerby, D. F. McMorrow, T. Strässle, S. Klotz, G. Hamel, R. A. Sadykov, V. Pomjakushina, M. Boehm, M. Jiménez-Ruiz, A. Schneidewind, E. Pomjakushina, M. Stingaciu, K. Conder, and H. M. Rønnow, 4-spin plaquette singlet state in the Shastry-Sutherland compound $\text{SrCu}_2(\text{BO}_3)_2$, *Nat. Phys.* **13**, 962 (2017).
- [29] J. Guo, G. Sun, B. Zhao, L. Wang, W. Hong, V. A. Sidorov, N. Ma, Q. Wu, S. Li, Z. Y. Meng, A. W. Sandvik, and L. Sun, Quantum phases of $\text{SrCu}_2(\text{BO}_3)_2$ from high-pressure thermodynamics, *Phys. Rev. Lett.* **124**, 206602 (2020).
- [30] S. Bettler, L. Stoppel, Z. Yan, S. Gvasaliya, and A. Zheludev, Sign switching of dimer correlations in $\text{SrCu}_2(\text{BO}_3)_2$ under hydrostatic pressure, *Phys. Rev. Res.* **2**, 012010(R) (2020).
- [31] J. L. Jimenez, S. P. G. Crone, E. Fogh, M. E. Zayed, R. Lortz, E. Pomjakushina, K. Conder, A. M. Läuchli, L. Weber, S. Wessel, A. Honecker, B. Normand, C. Ruegg, P. Corboz, H. M. Ronnow, and F. Mila, A quantum magnetic analogue to the critical point of water, *Nature (London)* **592**, 370 (2021).
- [32] Y. Cui, L. Liu, H. Lin, K.-H. Wu, W. Hong, X. Liu, C. Li, Z. Hu, N. Xi, S. Li, R. Yu, A. W. Sandvik, and W. Yu, Proximate deconfined quantum critical point in $\text{SrCu}_2(\text{BO}_3)_2$, *Science* **380**, 1179 (2023).
- [33] C. Boos, S. P. G. Crone, I. A. Niesen, P. Corboz, K. P. Schmidt, and F. Mila, Competition between intermediate plaquette phases in $\text{SrCu}_2(\text{BO}_3)_2$ under pressure, *Phys. Rev. B* **100**, 140413(R) (2019).
- [34] Z. Shi, S. Dissanayake, P. Corboz, W. Steinhart, D. Graf, D. M. Silevitch, H. A. Dabkowska, T. F. Rosenbaum, F. Mila, and S. Haravifard, Discovery of quantum phases in the Shastry-Sutherland compound $\text{SrCu}_2(\text{BO}_3)_2$ under extreme conditions of field and pressure, *Nat. Commun.* **13**, 2301 (2022).
- [35] A. Läuchli, S. Wessel, and M. Sigrist, Phase diagram of the quadrumerized Shastry-Sutherland model, *Phys. Rev. B* **66**, 014401 (2002).
- [36] P. Corboz and F. Mila, Tensor network study of the Shastry-Sutherland model in zero magnetic field, *Phys. Rev. B* **87**, 115144 (2013).
- [37] J. Y. Lee, Y.-Z. You, S. Sachdev, and A. Vishwanath, Signatures of a deconfined phase transition on the Shastry-Sutherland lattice: Applications to quantum critical $\text{SrCu}_2(\text{BO}_3)_2$, *Phys. Rev. X* **9**, 041037 (2019).
- [38] J. Yang, A. W. Sandvik, and L. Wang, Quantum criticality and spin liquid phase in the Shastry-Sutherland model, *Phys. Rev. B* **105**, L060409 (2022).
- [39] A. Keleş and E. Zhao, Rise and fall of plaquette order in the Shastry-Sutherland magnet revealed by pseudofermion functional renormalization group, *Phys. Rev. B* **105**, L041115 (2022).
- [40] L. Wang, Y. Zhang, and A. W. Sandvik, Quantum spin liquid phase in the Shastry-Sutherland model detected by an improved level spectroscopic method, *Chin. Phys. Lett.* **39**, 077502 (2022).
- [41] S. R. White, Density matrix formulation for quantum renormalization groups, *Phys. Rev. Lett.* **69**, 2863 (1992).
- [42] U. Schollwöck, The density-matrix renormalization group in the age of matrix product states, *Ann. Phys.* **326**, 96 (2011).
- [43] C. Nayak, S. H. Simon, A. Stern, M. Freedman, and S. Das Sarma, Non-Abelian anyons and topological quantum computation, *Rev. Mod. Phys.* **80**, 1083 (2008).
- [44] H. Li and F. D. M. Haldane, Entanglement spectrum as a generalization of entanglement entropy: Identification of topological order in non-Abelian fractional quantum Hall effect states, *Phys. Rev. Lett.* **101**, 010504 (2008).
- [45] X. G. Wen, F. Wilczek, and A. Zee, Chiral spin states and superconductivity, *Phys. Rev. B* **39**, 11413 (1989).
- [46] G. Baskaran, Novel local symmetries and chiral-symmetry-broken phases in $S=1/2$ triangular-lattice Heisenberg model, *Phys. Rev. Lett.* **63**, 2524 (1989).

- [47] D. Sen and R. Chitra, Large- U limit of a Hubbard model in a magnetic field: Chiral spin interactions and paramagnetism, *Phys. Rev. B* **51**, 1922 (1995).
- [48] R. Samajdar, M. S. Scheurer, S. Chatterjee, H. Guo, C. Xu, and S. Sachdev, Enhanced thermal Hall effect in the square-lattice Néel state, *Nat. Phys.* **15**, 1290 (2019).
- [49] S. R. White and A. L. Chernyshev, Néel order in square and triangular lattice Heisenberg models, *Phys. Rev. Lett.* **99**, 127004 (2007).
- [50] Y. Huang, W. Zhu, S.-S. Gong, H.-C. Jiang, and D. N. Sheng, Coexistence of non-Abelian chiral spin liquid and magnetic order in a spin-1 antiferromagnet, *Phys. Rev. B* **105**, 155104 (2022).
- [51] W.-W. Luo, Y. Huang, D. N. Sheng, and W. Zhu, Global quantum phase diagram and non-Abelian chiral spin liquid in a spin- $\frac{3}{2}$ square-lattice antiferromagnet, *Phys. Rev. B* **108**, 035130 (2023).
- [52] Z. Zhang and P. Sengupta, Generalized plaquette state in the anisotropic Shastry-Sutherland model, *Phys. Rev. B* **92**, 094440 (2015).
- [53] B. Zhao, P. Weinberg, and A. W. Sandvik, Symmetry-enhanced discontinuous phase transition in a two-dimensional quantum magnet, *Nat. Phys.* **15**, 678 (2019).
- [54] Y. Zhang, T. Grover, A. Turner, M. Oshikawa, and A. Vishwanath, Quasiparticle statistics and braiding from ground-state entanglement, *Phys. Rev. B* **85**, 235151 (2012).
- [55] W. Zhu, D. N. Sheng, and F. D. M. Haldane, Minimal entangled states and modular matrix for fractional quantum Hall effect in topological flat bands, *Phys. Rev. B* **88**, 035122 (2013).
- [56] S. Dong, E. Fradkin, R. G. Leigh, and S. Nowling, Topological entanglement entropy in Chern-Simons theories and quantum Hall fluids, *J. High Energy Phys.* **05** (2008) 016.
- [57] P. Fendley, M. P. A. Fisher, and C. Nayak, Topological entanglement entropy from the holographic partition function, *J. Stat. Phys.* **126**, 1111 (2007).
- [58] E. Rowell, R. Stong, and Z. Wang, On classification of modular tensor categories, *Commun. Math. Phys.* **292**, 343 (2009).
- [59] P. D. Francesco, P. Mathieu, and D. Sénéchal, *Conformal Field Theory* (Springer, New York, 1997).
- [60] B. A. Bernevig and F. D. M. Haldane, Model fractional quantum Hall states and Jack polynomials, *Phys. Rev. Lett.* **100**, 246802 (2008).
- [61] B. Wang, M. Feng, and Z.-Q. Chen, Berezinskii-Kosterlitz-Thouless transition uncovered by the fidelity susceptibility in the XXZ model, *Phys. Rev. A* **81**, 064301 (2010).
- [62] W.-L. You and Y.-L. Dong, Fidelity susceptibility in two-dimensional spin-orbit models, *Phys. Rev. B* **84**, 174426 (2011).
- [63] S.-J. Gu, Fidelity approach to quantum phase transitions, *Int. J. Mod. Phys. B* **24**, 4371 (2010).
- [64] K. Okamoto and K. Nomura, Fluid-dimer critical point in $S = 12$ antiferromagnetic Heisenberg chain with next nearest neighbor interactions, *Phys. Lett. A* **169**, 433 (1992).
- [65] S. Eggert, Numerical evidence for multiplicative logarithmic corrections from marginal operators, *Phys. Rev. B* **54**, R9612 (1996).
- [66] L. Wang and A. W. Sandvik, Critical level crossings and gapless spin liquid in the square-lattice spin-1/2 $J_1 - J_2$ Heisenberg antiferromagnet, *Phys. Rev. Lett.* **121**, 107202 (2018).
- [67] F. Ferrari and F. Becca, Gapless spin liquid and valence-bond solid in the $J_1 - J_2$ Heisenberg model on the square lattice: Insights from singlet and triplet excitations, *Phys. Rev. B* **102**, 014417 (2020).
- [68] Y. Nomura and M. Imada, Dirac-type nodal spin liquid revealed by refined quantum many-body solver using neural-network wave function, correlation ratio, and level spectroscopy, *Phys. Rev. X* **11**, 031034 (2021).
- [69] A. W. Sandvik, Continuous quantum phase transition between an antiferromagnet and a valence-bond solid in two dimensions: Evidence for logarithmic corrections to scaling, *Phys. Rev. Lett.* **104**, 177201 (2010).
- [70] H. Suwa and S. Todo, Generalized moment method for gap estimation and quantum Monte Carlo level spectroscopy, *Phys. Rev. Lett.* **115**, 080601 (2015).
- [71] H. Suwa, A. Sen, and A. W. Sandvik, Level spectroscopy in a two-dimensional quantum magnet: Linearly dispersing spinons at the deconfined quantum critical point, *Phys. Rev. B* **94**, 144416 (2016).
- [72] M. Mambrini, A. Läuchli, D. Poilblanc, and F. Mila, Plaquette valence-bond crystal in the frustrated Heisenberg quantum antiferromagnet on the square lattice, *Phys. Rev. B* **74**, 144422 (2006).
- [73] S. Banerjee, W. Zhu, and S.-Z. Lin, Electromagnetic signatures of a chiral quantum spin liquid, *npj Quantum Mater.* **8**, 63 (2023).